Phonon-assisted coherent transport of excitations in Rydberg-dressed atom arrays

Arkadiusz Kosior[,1] Servaas Kokkelmans,[2] Maciej Lewenstein,[3,4] Jakub Zakrzewski[,5,6] and Marcin Płodzień[3]

[1]*Institute for Theoretical Physics, University of Innsbruck, 6020 Innsbruck, Austria*
[2]*Department of Applied Physics, Eindhoven University of Technology, PO Box 513, 5600 MB Eindhoven, The Netherlands*
[3]*Institut de Ciencies Fotoniques, The Barcelona Institute of Science and Technology, 08860 Castelldefels, Barcelona, Spain*
[4]*ICREA, Passeig Lluis Companys 23, 08010 Barcelona, Spain*
[5]*Instytut Fizyki Teoretycznej, Uniwersytet Jagielloński, Łojasiewicza 11, 30-348 Kraków, Poland*
[6]*Mark Kac Center for Complex Systems Research, Jagiellonian University, Łojasiewicza 11, 30-348 Kraków, Poland*

Polarons, which arise from the self-trapping interaction between electrons and lattice distortions in a solid, have been known and extensively investigated for nearly a century. Nevertheless, the study of polarons continues to be an active and evolving field, with ongoing advancements in both fundamental understanding and practical applications. Here, we present a microscopic model that exhibits a diverse range of dynamic behavior, arising from the intricate interplay between two excitation-phonon coupling terms. The derivation of the model is based on an experimentally feasible Rydberg-dressed system with dipole-dipole interactions, making it a promising candidate for realization in a Rydberg atoms quantum simulator for excitation dynamics interacting with optical phonons. Remarkably, our analysis reveals a growing asymmetry in Bloch oscillations, leading to a macroscopic transport of nonspreading excitations under a constant force. Finally, we demonstrate the robustness of our findings against on-site random potential.

I. INTRODUCTION

Polarons are quasiparticles that emerge from the coupling between electrons (or holes) with ions of a crystalline structure in polarizable materials. The idea of electron self-trapping due to lattice deformations dates back to Landau's seminal 1933 paper [1], but the modern concept of a polaron as an electron dressed by phonons was formulated in 1946 by Pekar and developed later by Fröhlich [2], Feynman [3,4], Holstein [5], and Su, Schrieffer, and Heeger [6–8]. Since their discovery, polarons have been extensively investigated, both theoretically and experimentally, not only in the field of condensed matter physics (for reviews see Refs. [9,10]), but also in various chemical and biological contexts, e.g., in protein propagation [11–13]. In particular, in the modeling of charge migration in DNA molecules, it is assumed that a localized polaron is formed in the helix near a base due to an interaction between a charge carrier and a phonon. When a uniform electric field is applied, the polaron moves at a constant velocity and a current flows through the chain [14–16]. The charge carrier transport takes place due to coupling between carrier and phonons; in contrast, in the absence of phonons, an external constant force induces Bloch oscillations [17–19], where the mean position of the carrier is constant while its width periodically changes in time.

Polarons have been studied in many, seemingly different experimental setups, ranging from ultracold ions [20–23], polar molecules [24–27], mobile impurities in Bose and Fermi gases [28–30], ultracold dipolar and Rydberg atoms [31–39], to quantum dots on a carbon nanotube [40]. Although each of these platforms possesses its unique strengths and benefits, recently there has been an exceptional outburst of interest in quantum simulation and computation with Rydberg atoms, which provide a remarkable level of flexibility for executing quantum operations and constructing quantum many-body Hamiltonians [41]. While the latter can contribute to our comprehension of the static properties of many-body systems, their main benefits are centered around exploring the complex dynamics displayed by these systems. In particular, in the context of polarons, it has been demonstrated that the dipole-dipole interactions between distinct Rydberg-dressed states can result in coherent quantum transport of electronic-like excitations [31], which can further be coupled to optical phonons [32]. The paradigmatic one-dimensional topological Su-Schrieffer-Heeger (SSH) model [6] describing the soliton formation in long-chain polyacetylene due to excitation-phonon coupling, has been realized in Rydberg arrays [42–44].

In this paper, we continue along this path and present theoretical studies of an implementation of a microscopic model featuring the interplay of SSH and Fröhlich electron-phonon coupling mechanisms between optical phonons and excitations, under the influence of an external force and disorder. In particular, we focus on the directional transport of an excitation interacting with phonons. We indicate an excitation-phonon coupling regime where the competition between Bloch oscillations and interactions results in the coherent transport of a well-localized wave packet over a long distance. We show the robustness of such a coherent transport of well-localized wave packets to the on-site random potential, indicating that a relatively strong disorder does not affect significantly the transport properties. Moreover, for completeness, we consider also excitation coupling to acoustic phonons.

The paper is divided into three parts. In the first part, Sec. II, we describe the physical setup and derive the effective Hamiltonian in Rydberg-dressed atomic arrays. The second part, described in Sec. III, focuses on the dynamics of the system under experimentally relevant parameters. In this section, we observe the macroscopic transport of the center of mass and a transition between Bloch oscillations and moving polaron regimes. In the third part, Sec. IV, we comprehensively analyze the previously derived microscopic model, which exhibits a rich phase diagram due to the interplay of two different electron-phonon coupling mechanisms. Finally, we compare the behavior of excitations with acoustic and optical phonons and demonstrate the robustness of our results.

II. MODEL AND ITS HAMILTONIAN

We consider a one-dimensional chain of N equidistant Rydberg atoms with lattice constant x_0 and positions $x_j = j x_0$, confined in a periodic trap, implemented either by an optical lattice [45,46], an optical tweezer array [47–49], a Rydberg microtrap [50], or a painted potential [51]. We assume that the spatial motion of the atoms is suppressed by the strong confinement of each Rydberg atom in local potential minima. Although the atomic motion is frozen, it is remarkable that such a Rydberg system can display highly nontrivial dynamics. In particular, the induced dipole-dipole interactions between distinct Rydberg-dressed states can lead to the emergence of coherent quantum transport of electronic-like excitations [31]. In the following, we first briefly repeat the derivation of the Hamiltonian that characterizes the dynamics of single excitations [31]. The purpose of this recap is to modify the setup to incorporate nearly arbitrary on-site potential terms. Next, after introducing phonons into the system [32], we derive an effective nearest-neighbor Hamiltonian that includes two excitation-phonon coupling terms, which we comprehensively study in the forthcoming sections, focusing on the dynamics in the presence of an external constant field.

A. Single-excitation Hamiltonian in arbitrary potentials

We assume that each Rydberg atom can be initially found in one of the ground-state hyperfine levels, $|g\rangle$ or $|g'\rangle$. By applying far-detuned dressing laser fields, with effective Rabi frequencies Ω_s, Ω_p and detunings Δ_s, Δ_p, respectively, these two hyperfine states can be coherently coupled to selected highly excited Rydberg states, $|s\rangle$ or $|p\rangle$, with principal quantum number $n \gg 1$ and different angular momenta. Consequently, each atom can be found in one of the two Rydberg dressed states [31,46,52–55], which are a slight admixture of Rydberg states to the atomic ground states

$$|0\rangle_j \approx |g\rangle_j + \alpha_s |s\rangle_j \quad \text{or} \quad |1\rangle_j \approx |g'\rangle_j + \alpha_p |p\rangle_j, \quad (1)$$

with $\alpha_{s/p} = \Omega_{s/p}/[2\Delta_{s/p}]$ and j denoting the position of an atom. Treating α_s, α_p as perturbation parameters in van Vleck perturbation theory, Wüster *et al.* [31] showed that the dipole-dipole interaction can exchange the internal states of a neighboring pair, e.g., $|1\rangle_1|0\rangle_2 \rightarrow |0\rangle_1|1\rangle_2$. This process can be viewed as a hopping of an excitation from $j = 1$ to $j = 2$ lattice site, which conserves the number of excitations.

The perturbation analysis can be extended to a chain of N atoms, where the effective Hamiltonian in the single-excitation manifold (up to the fourth order in α_s and α_p) reads [31,32]

$$\hat{H}_0 = \sum_j \hat{n}_j (E_2 + E_4 + A_j) + \sum_{j,k} A_{jk} \hat{a}_j^\dagger \hat{a}_k, \quad (2)$$

where $\hat{a}_j$ ($\hat{a}_j^\dagger$) denote an annihilation (creation) operator of excitation on site j, while

$$A_j = \hbar \alpha_s^2 \alpha_p^2 \left(\sum_{k \neq j} \frac{1}{1 - \bar{U}_{kj}^2} \right) (\Delta_s + \Delta_p), \quad (3a)$$

$$A_{jk} = \hbar \alpha_s^2 \alpha_p^2 \frac{\bar{U}_{jk}}{1 - \bar{U}_{jk}^2} (\Delta_s + \Delta_p), \quad (3b)$$

with $\bar{U}_{jk} = C_3/[\hbar |x_i - x_j|^3 (\Delta_s + \Delta_p)]$ and C_3 quantifying the transition dipole moment between the Rydberg states, describe perturbative dipole-dipole interactions. Finally, E_2 and E_4 are constant energy shifts of the second and fourth order, respectively,

$$E_2/\hbar = (N - 1)\alpha_s^2 \Delta_s + \alpha_p^2 \Delta_p, \quad (4a)$$

$$E_4/\hbar = (N - 1)\alpha_s^4 \Delta_s + \alpha_p^4 \Delta_p$$
$$+ (N - 1)\alpha_s^2 \alpha_p^2 (\Delta_s + \Delta_p). \quad (4b)$$

Although in principle constant energy terms could be always ignored as they do not contribute to the dynamics of excitations, let us consider now a scenario where the Rabi frequency Ω_p depends on the atomic position on the lattice, i.e., we assume that

$$\Omega_p \rightarrow \Omega_p(j) \equiv \Omega_p[1 + \delta\Omega(j)], \quad (5)$$

where $\delta\Omega(j)$ is arbitrary, but small correction of the order $(\alpha_{p/s})^2$. With this assumption, and by retaining terms up to the fourth order, the effective Hamiltonian in Eq. (2) acquires an additional term, namely,

$$\hat{H} = \hat{H}_0 + \hbar \alpha_p^2 \Delta_p \sum_j \delta\Omega(j) \hat{n}_j. \quad (6)$$

Because the term proportional to $\alpha_p^2 \delta\Omega(j)$ is of the same order as A_j, it can be incorporated into the definition of A_j in Eq. (3a). With this simple modification, we gained a position-dependent effective potential term that can strongly affect the dynamics of excitations. Although the potential term can be tailored almost arbitrarily, from now on we consider one of its simplest forms, i.e., we choose

$$\delta\Omega(j) = 2\alpha_s^2 (F j + \epsilon_j). \quad (7)$$

The first term in the parentheses being linearly proportional to position j emulates the presence of a constant external field F. The second term, with ϵ_j being a random variable, gives rise to the on-site potential disorder. Note that both terms lead to localization of the excitation either due to Stark localization [17] in a constant tilt F or Anderson localization [56] due to random ϵ_j. As explained in the next part, the situation is not so straightforward.

B. Excitation-phonon Hamiltonian

In this part, we relax our previous assumption that the atoms of the array are completely immobile. Although we still assume that no atom can move through the lattice, we now let them vibrate in the vicinity of their local equilibrium points. This will affect, as we shall see, the dynamics of excitations. We consider now a scenario where an atom in the jth lattice site and with mass m may oscillate with a frequency $\omega_0 = \sqrt{k/m}$ inside a local potential well, that can be approximated by a quadratic potential

$$\frac{k}{2}(x - jx_0)^2 \equiv \frac{kx_0^2}{2}(u_j)^2, \tag{8}$$

with k being the force constant and where u_j denotes dimensionless distortion from the local equilibrium position. The motion of atoms can be quantized $u_j \to \hat{u}_j$ and described by a simple quantum harmonic oscillator. This vibrational motion is responsible for the distortion of an atomic array and can be considered as a phonon. Since the Hamiltonian of the previous section describing the motion of single excitations strongly depends on the position of atoms, phonons can propagate through space due to the coupling to excitations. Before proceeding to derive the effective Hamiltonian of the system with phonon-excitation coupling, for clarity and simplicity we assume that

$$\alpha \equiv \alpha_s = \alpha_p, \quad \Delta \equiv \Delta_s = \Delta_p. \tag{9}$$

Moreover, from now on we also fix the timescales and energy scales and go to the dimensionless units by dividing all the energy scales by $2\hbar\alpha^4\Delta$.

Although the setup described in Sec. II A admits only dispersionless optical phonons that correspond to local vibrations of atoms around local minima, we consider here two different types of phonons. We proceed by writing the phononic Hamiltonian explicitly in terms of the dimensionless position and momentum operators $\hat{u}_j$, $\hat{p}_j$ of local distortions

$$\hat{H}_{\text{ph}} = \sum_j \frac{\hat{p}_j^2}{2m_{\text{eff}}} + \frac{m_{\text{eff}}\omega_{\text{eff}}^2}{2}(\hat{u}_j - \eta\hat{u}_{j-1})^2, \tag{10}$$

with the effective dimensionless mass

$$m_{\text{eff}} = 2mx_0^2\alpha^4\Delta/\hbar, \tag{11}$$

and the effective oscillator frequency

$$\omega_{\text{eff}} = \omega_0/(2\alpha^4\Delta), \quad \omega_0 = \sqrt{k/m}, \tag{12}$$

where ω_0 is the bare frequency. By changing the parameter η in Eq. (10), diverse phonon types can be achieved. In particular, $\eta = 0$ corresponds to the aforementioned local vibrations (i.e., dispersionless optical phonons) and $\eta = 1$ describes acoustic phonons. These two phonon types are characterized by the dispersion relation

$$\epsilon_q = \begin{cases} \omega_{\text{eff}}, & \text{(optical phonons, } \eta = 0), \\ 2\omega_{\text{eff}}|\sin(qx_0/2)|, & \text{(acoustic phonons, } \eta = 1), \end{cases} \tag{13}$$

which can be readily found by writing the phononic Hamiltonian (10) in terms of its eigenmodes

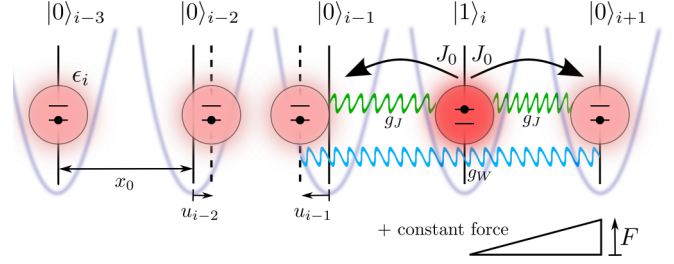$$\hat{H}_{\text{ph}} = \sum_q \epsilon_q \left(\hat{b}_q^\dagger \hat{b}_q + \frac{1}{2}\right), \tag{14}$$

FIG. 1. Schematic illustration of all processes in the effective Hamiltonian $\hat{H}_{\text{eff}}$ in Eq. (16), describing the dynamics of a single excitation in a one-dimensional array of Rydberg atoms located at $x_0(j + u_j)$, with u_j being a dimensionless distortion from an equilibrium position. $\hat{H}_{\text{ex}}$ describes a bare hopping (in the limit $u_j \to 0$) of an excitation at site j to its neighboring sites with amplitude J_0 in the presence of a constant force F and on-site disorder ϵ_j, see Eq. (17). The effective hopping and on-site potential is further modified by the phonon couplings g_J and g_W, respectively, see Eq. (19).

where $\hat{b}_q^\dagger$ ($\hat{b}_q$) creates (annihilates) the phonon with quasi-momentum q, and are related to the local dimensionless momentum and position operators $\hat{p}_i$, $\hat{u}_i$ of distortion by

$$\hat{u}_j = \sum_q \frac{1}{\sqrt{2N\epsilon_q m_{\text{eff}}}}(\hat{b}_q + \hat{b}_{-q}^\dagger)e^{iqjx_0},$$

$$\hat{p}_j = -i\sum_q \sqrt{\frac{\epsilon_q m_{\text{eff}}}{2N}}(\hat{b}_q - \hat{b}_{-q}^\dagger)e^{iqjx_0}. \tag{15}$$

Having discussed the phononic degrees of freedom, we can now write the fully effective Hamiltonian governing the motion of single excitations coupled to phonons. The derivation is straightforward and requires (i) the expansion of the position-dependent coefficients [given by Eq. (3)] in the Hamiltonian (6) of the previous section up to the first order in $\hat{u}_j$, and (ii) dropping the next-to-nearest neighbor contributions [57]. By following these steps, we obtain the effective excitation-phonon Hamiltonian (cf. Fig. 1), which consists of four parts, i.e.,

$$\hat{H}_{\text{eff}} = \hat{H}_{\text{ph}} + \hat{H}_{\text{ex}} + \hat{H}_{\text{J}} + \hat{H}_{\text{W}}, \tag{16}$$

where $\hat{H}_{\text{ph}}$ is the phononic Hamiltonian Eq. (10)

$$\hat{H}_{\text{ex}} = J_0(\hat{a}_{j+1}^\dagger\hat{a}_j + \text{H.c.}) + \sum_j (jF + \epsilon_j)\hat{a}_j^\dagger\hat{a}_j, \tag{17}$$

describes excitations with the hopping amplitude

$$J_0 = \kappa/(1 - \kappa^2), \quad \kappa = C_3/(2\hbar\Delta x_0^3), \tag{18}$$

experiencing an external constant force F and a local on-site disorder ϵ_j. Finally,

$$\hat{H}_{\text{J}} = g_J \sum_j (\hat{u}_{j+1} - \hat{u}_j)\hat{a}_{j+1}^\dagger\hat{a}_j + \text{H.c.}, \tag{19a}$$

$$\hat{H}_{\text{W}} = g_W \sum_j (\hat{u}_{j+1} - \hat{u}_{j-1})\hat{a}_j^\dagger\hat{a}_j, \tag{19b}$$

are the notable SSH and Fröhling Hamiltonians [6,10], respectively, that correspond to two different mechanisms of

excitation-phonon couplings, with dimensionless coupling parameters

$$g_J = -3\kappa(1 + \kappa^2)/(\kappa^2 - 1)^2, \tag{20a}$$

$$g_W = -6\kappa^2/(\kappa^2 - 1)^2. \tag{20b}$$

C. Equations of motion

The full numerical analysis of the polaron dynamics on the many-body level is one of the most challenging computational tasks due to the nonconserved total number of phonons in the system, which prevents it from working in a restricted, fixed particle-number Hilbert space sector of the phononic degrees of freedom. Additionally, even without a force F the effective Hamiltonian of the systems (16) depends, in principle, on many parameters, namely, $J_0, g_W, g_J, \omega_{\text{eff}}$, and m_{eff}, making the full analysis of the system even more challenging.

To analyze the dynamical properties of the considered system, in the following we make the semiclassical approximation by applying the Davydov ansatz [58–64], which relies on two fundamental assumptions: (i) treating phononic oscillations classically and (ii) representing solutions as separable states without entanglement between quantum-like excitations and classical-like phonons. In other words, we assume that phonons are in a coherent state and that the full wave function is a product state of the excitation and coherent phonons part, as

$$|\Psi(t)\rangle = \left(\sum_j \psi_j(t)\hat{a}_j^\dagger \right) \otimes \left(e^{-i\sum_j[u_j(t)\hat{p}_j - p_j(t)\hat{u}_j]} \right)|\texttt{vac}\rangle,$$
$$\tag{21}$$

where $|\psi_j(t)|^2$ is a probability of finding an excitation at a site j, $u_j(t)$, and $p_j(t)$ are expectation values of phononic position and momentum operators. The equation of motion for $\psi_j(t)$ and $u_j(t)$ can be subsequently derived from a classical conjugate variable Heisenberg equations of motions using the generalized Ehrenfest theorem, see, for example, Ref. [13]. By following these steps, we obtain a closed set of coupled differential equations for the excitation amplitude $\psi_j(t)$ and classical field $u_j(t)$. The equations can be written in a concise form, as

$$i\dot{\psi}_j = J_j\psi_{j+1} + J_{j-1}\psi_{j-1} + W_j\psi_j, \tag{22a}$$

$$\ddot{u}_j = -\omega_{\text{eff}}^2 \mathcal{D}[\{u_j\}] + \mathcal{S}[\{\psi_j\}], \tag{22b}$$

where the effective potential experienced by an excitation $W_j(t)$ and the effective hopping amplitude $J_j(t)$ are both time-dependent functions due to the coupling to the gradient of the phononic field $u_j(t)$, i.e.,

$$W_j(t) = jF + \epsilon_j + g_W[u_{j+1}(t) - u_{j-1}(t)],$$
$$J_j(t) = J_0 + g_J[u_{j+1}(t) - u_j(t)]. \tag{23}$$

As such, both $W_j(t)$ and $J_j(t)$ are responsible for the self-trapping of an excitation. Similarly, the phononic equation (22b) also depends on the excitation amplitude $\psi_i(t)$

through the $\mathcal{S}[\{\psi_j\}]$ operator, given by

$$\mathcal{S}[\{\psi_j\}] = -\frac{g_W}{m_{\text{eff}}}(|\psi_{j+1}|^2 - |\psi_{j-1}|^2)$$
$$- \frac{g_J}{m_{\text{eff}}}[\psi_j^*(\psi_{j+1} - \psi_{j-1}) + \text{c.c.}], \tag{24}$$

which acts as a time-dependent source for the phonon field $u_j(t)$. Finally, the phononic dispersion relation, given by Eq. (13), is necessarily present in the phononic equation through the $\mathcal{D}[\{u_j\}]$ operator

$$\mathcal{D}[\{u_j\}] = \begin{cases} u_j, & \eta = 0, \\ 2u_j - u_{j+1} - u_{j-1}, & \eta = 1, \end{cases} \tag{25}$$

which introduces a crucial difference in the propagation of optical ($\eta = 0$) and acoustic ($\eta = 1$) phonons [65], which we investigate in the next sections.

D. Analyzed observables

Throughout this article we choose the initial conditions $\psi_j(0) = \delta_{j,0}$ and $u_j(0) = \dot{u}_j(0) = 0$ for the equations of motion, Eq. (22), that correspond to a single excitation on a central lattice site and initially unperturbed lattice. Without a phonon coupling and for $F = 0$, these initial conditions simply correspond to a quantum particle that spreads symmetrically in both lattice directions characterized by a constant Lieb-Robinson velocity [66], so that its center of mass remains localized at the initial position. Contrary to the classical case, a quantum particle on a lattice will not even move in the presence of a constant force F, but instead it starts to perform Bloch oscillations [67]. The situation is different in interacting systems, either in a case of particle-particle interactions [18], which may further lead to disorder-free many-body localization [68–77], or in the presence of phonons, which can induce transient polarons at the end of Bloch oscillation periods [62,78] (see also Ref. [79]).

In this study, we investigate how the propagation of a single excitation is influenced by the two competing phonon-coupling mechanisms under the applied, constant force. Specifically, we aim at answering the two following questions: (i) how much does the excitation spread due to the coupling with phonons and (ii) does its center of mass move in the presence of the constant force F? To respond to these questions we focus on three simple observables that can be calculated based on the local density measurements. First, we consider the participation ratio (R_P), defined as [80]

$$R_P(t) = \left(\sum_j |\psi_j(t)|^4 \right)^{-1}, \tag{26}$$

where we assume a unit normalization of the wave function $\sum_j |\psi_j|^2 = 1$. The participation ratio R_P is equal to 1 where excitation is localized on a single lattice site and equals N when is completely delocalized over the entire lattice. The second observable is the center-of-mass position of the wave packet, i.e.,

$$x(t) = \sum_{j=-N/2}^{N/2} j|\psi_j(t)|^2. \tag{27}$$

Moreover, in some cases, analyzing the ratio of the two quantities mentioned above can provide valuable insights. We define this ratio, denoted as ξ, as

$$\xi(t) = \frac{|x(t)|}{R_P(t)}. \qquad (28)$$

ξ is a quantity ranging from 0 to $\xi_{max} = N/2$. The maximum value ξ_{max} corresponds to a moving, maximally localized, nondispersive solution that has reached the boundary of the system. As such, ξ can be viewed as an indicative measure for selecting well-localized solutions moving in one direction.

Finally, it is worth mentioning that it is often not necessary to analyze the entire time range of the above observables. In fact, to discern various dynamic behaviors, it is usually sufficient to look at $R_P(t)$, $x(t)$, and $\xi(t)$ at the final evolution time $t_f \gg 1$. For example, large $R_P(t_f)$ (relative to the system size N) suggests that excitation is not stable and has delocalized over a lattice.

III. POLARON DYNAMICS: EXPERIMENTAL CONSIDERATIONS

In this section we elaborate on the results of the previous sections and study the dynamics of a Rydberg excitation under the presence of the external force F, solving the equations of motion for a physically relevant range of parameters. The effective Hamiltonian (16) of the system relies on several effective, dimensional parameters, including $m_{eff} = 2mx_0^2\alpha^4\Delta/\hbar$, $\omega_{eff} = \omega_0/(2\alpha^4\Delta)$, as well as J_0, g_J, g_W, given by Eqs. (18) and (20). However, it is worth noting that the later three parameters are not independent within our setup, and their values are determined by a single parameter $\kappa = C_3/(2\hbar\Delta x_0^3)$. This provides us with significant flexibility in selecting appropriate physical parameters for our convenience. We stress that the proposed quantum simulator allows for simulating excitation coupled to optical phonons only.

In the following, we choose the highly excited Rydberg states $|s\rangle$, $|p\rangle$ of Ru-87 with principal quantum number $n = 50$ and angular momentum equal to 0 or $\hbar$, for which $C_3 = 3.224$ GHz $\times$ μm^{-3}. We fix the lattice spacing $x_0 = 2$ μm, and the local trap frequency $\omega_0 = 20$ kHz. In the numerical simulations, we vary the dimensionless parameter κ between 0.80–0.86, which is equivalent to the change of the detuning $\Delta \sim 234$–252 MHz, and corresponds to the dressing parameter $\alpha \sim 0.04$. Importantly, by increasing κ we also increase the phonon coupling strength from around $g_J/m_{eff} \sim g_W/m_{eff} \sim -4.5$ to $g_J/m_{eff} \sim g_W/m_{eff} \sim -8$. Furthermore, we remind the reader that in our setup only the optical phonons (i.e., dispersionless vibrations) are experimentally relevant and, therefore, in this section we set $\eta = 0$. Finally, we fix the value of the force at $F = 0.2$, and we choose the system size to $N = 401$.

To characterize the transport properties of an excitation $\psi_i(t)$, in the top panel of Fig. 2 we plot its center-of-mass position $x(t)$ and the corresponding participation ratio $R_P(t)$, see Eqs. (26) and (27) for the respective definitions. In the bottom panel, we additionally illustrate the ratio $\xi = |x|/R_P$. All these quantities are plotted as a function of κ, at a fixed time $t_f = 2.1\,T_B \approx 66$, where $T_B = 2\pi/F$ is the Bloch oscillation period. We find that up to $\kappa \sim 0.83$ both $x(t_f)$ and $R_P(t_f)$ are
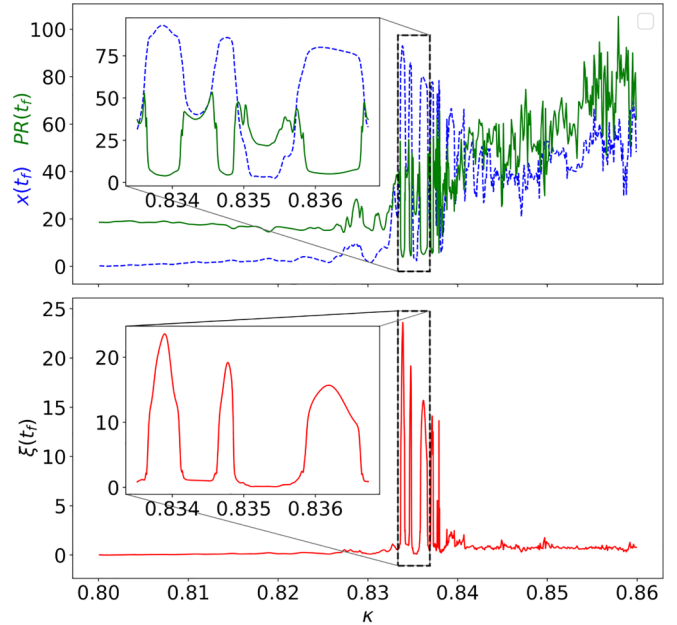

FIG. 2. The top panel illustrates the center of mass motion $x(t)$ of an excitation (dashed blue line) under a constant, external force $F = 0.2$, and the corresponding participation ratio $R_P(t)$ (solid green line), evaluated at the final evolution time t_f, and plotted as functions of the dimensionless parameter κ [see Eq. (16) and definitions below it]. In the bottom panel, the ratio $\xi = |x|/R_P$ is shown. The peaks in the plot correspond to parameter regimes where a well-localized excitation is transferred under the influence of a constant force F. All physical parameters have been chosen with careful consideration of their experimental relevance, as discussed in the main text. The time evolution range is $t \in [0, t_f]$, where the final time t_f is chosen as $t_f = 2.1\,T_B = 4.2\,\pi/F \approx 66$.

small (relative to the system size N) which corresponds to the Bloch oscillation-like dynamics where the phonon-influence is minimal. In contrast, phonons play important role above $\kappa \sim 0.83$ where the system dynamics is quite sensitive to the choice of microscopic parameters. Within the chaotic-like regime, the typical Bloch oscillation dynamics is completely disrupted, as the majority of solutions become delocalized across the lattice, leading to large values of $R_P(t)$. However, amidst this chaotic behavior, we also discover intervals of stability, characterized by peaks of $\xi(t_f)$, where a substantial portion of the wave packet becomes well localized and exhibits near-constant velocity of motion.

We illustrate those different dynamical behaviours in Fig. 3, where the first column, i.e., Figs. 3(a) to 3(d), show the time evolution of the excitation density $|\psi_j(t)|^2$, while the second column [Figs. 3(e) to 3(h)] illustrates the corresponding time evolution of the center-of-mass position $x(t)$ and the participation ratio $R_P(t)$. In the first row ($\kappa = 0.8$), we observe almost perfect Bloch oscillations. However, upon closer examination, a subtle asymmetry becomes apparent, which is evident by a nonzero $x(t)$. The asymmetry is enhanced for a higher $\kappa = 0.83$, as depicted in the second row of Fig. 3. Finally, the last two rows of Fig. 3 illustrate the time evolution of the excitation density in the chaotic-like regime above $\kappa \sim 0.83$, cf. Fig. 2, where most of the solutions
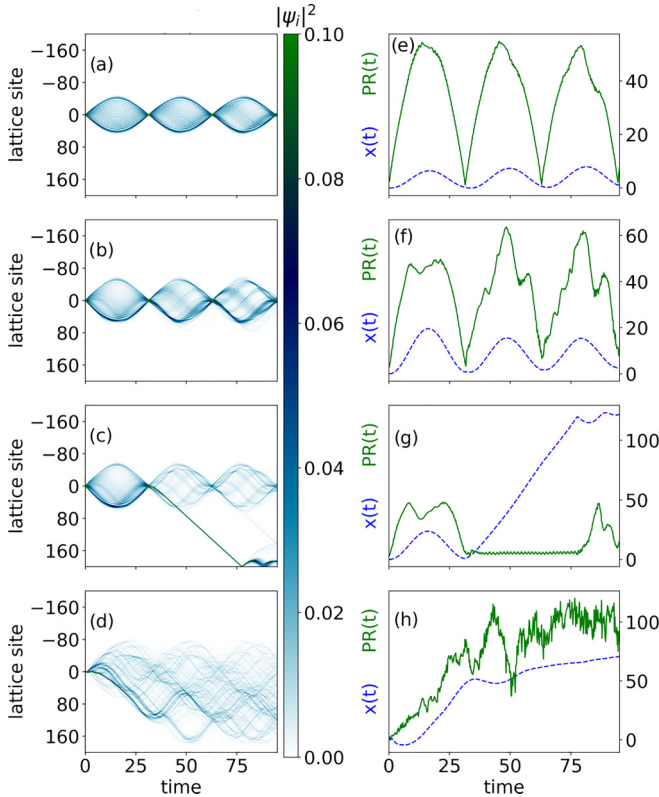
FIG. 3. The panels illustrate the diverse dynamic behaviors observed in our study. The (a)–(d) first column showcases the time evolution of the excitation density $|\psi_j(t)|^2$ (color encoded), while (e)–(h) the second column, panels illustrates the corresponding temporal changes in the center-of-mass position $x(t)$ (dashed blue lines) and the participation ratio $R_P(t)$ (solid green lines). In the first row ($\kappa = 0.8$), near-perfect Bloch oscillations are observed. However, upon closer examination, a subtle yet discernible asymmetry becomes apparent, as indicated by the nonzero value of $x(t)$. This asymmetry becomes more pronounced in the second row for a higher κ value of 0.83. The subsequent rows of the figure provide insights into the time evolution of the excitation density for the specific cases of a well-localized wave function ($\kappa = 0.834$) and a spreading wave function ($\kappa = 0.86$). These distinct parameter regimes highlight the contrasting behavior and spatial characteristics of the excitations. All physical parameters are the same as in Fig. 2.

are delocalized over a lattice, as in Fig. 3(d) for $\kappa = 0.86$. In contrast, in Fig. 3(c) we illustrate a regular behavior for $\kappa = 0.834$, which lies inside one of the aforementioned stability windows. In this scenario, due to constructive interference after one Bloch oscillation period, a prominent portion of the wave function coalesces into a very narrow nondispersive wave packet that moves with a nearly constant velocity. Overall, Fig. 3 offers a comprehensive visual representation of the dynamic phenomena investigated in this section, shedding light on the varying dynamical behaviors and properties of the system with increasing phonon interaction.

IV. DYNAMICAL PHASE DIAGRAMS OF THE EFFECTIVE HAMILTONIAN

In the previous sections, we derived and then analyzed a microscopic Hamiltonian (16), governing the dynamics

of an excitation coupled to phonons through two different mechanisms, i.e., the SSH and Fröhling Hamiltonians, see Eq. (19). While maintaining a close connection to the experimental platform, it is important to note that in the considered Rydberg setup, the phonon coupling strengths g_J and g_W are not independent. Instead, they can both be expressed in terms of a single parameter κ, as demonstrated in Eq. (20). Consequently, investigating the interplay between these two competing phonon-coupling mechanisms within the current Rydberg platform becomes challenging. To address this limitation and explore the complete phase diagram in a more general context, in this section, we treat g_J and g_W as completely independent and fix other parameters. In the initial phase, as described in Sec. IV A, our primary objective is to identify a stable polaron regime. Specifically, we aim to find a regime in which an initially localized excitation does not spread during the course of time evolution. Subsequently, in Sec. IV B, we demonstrate the existence of stable islands where polarons can exhibit nondispersive motion when subjected to a constant force, even in the presence of substantial disorder. Furthermore, in this part, we thoroughly examine the quantitative differences in dynamics of optical and acoustic phonons. In the following, we set the system size to $N = 401$ and solve the equations of motions in a fixed time interval $t \in [0, t_f = 16.5]$. Unless explicitly stated otherwise, we also set $m_{\text{eff}} = 0.5$, $\omega_{\text{eff}} = 10$, and $J_0 = 1$.

A. Polaron formation

In the preceding section, we already witnessed the emergence of a nondispersive, self-trapped polaron through the excitation-phonon coupling. Building upon this observation, here we independently vary the two coupling strengths, g_J, and g_W, to identify a stable polaron regime. It is worth noting that the Hamiltonian of the system, as described by Eq. (16), is invariant under the simultaneous transformation: $u_j \rightarrow -u_j$, $g_J \rightarrow -g_J$, and $g_W \rightarrow -g_W$. Therefore, without loss of generality, we can assume $g_J \geqslant 0$.

In Fig. 4, we present a phase diagram of the participation ratio R_P calculated at the final evolution time for a broad range of values $g_J \in [0, 45]$ and $g_W \in [-16, 20]$. Each panel of Fig. 4 corresponds to distinct values of m_{eff} and η, as specified in the figure caption. In terms of the layout, the left (right) column corresponds to the optical (acoustic) phonons and m_{eff} increases from top to bottom. In all panels of Fig. 4, we observe wide regions with both extended states (warm colors) and well-localized solutions (dark blue colors), with the latter corresponding to stable, stationary polarons. We discover a nontrivial dependence of the participation ratio on both coupling strengths. Moreover, we find qualitatively similar behavior for both types of phonon, however, the acoustic phonons exhibit greater dynamic stability. This is evident from the presence of a chaotic-like region (the light blue dotted area, compare with Fig. 2 and see the discussion in Sec. III). Finally, we indicate that a decrease of effective mass m_{eff} stabilizes the excitation supporting localized polaron formation.

B. Robustness of coherent transport against disorder

In this paragraph, we focus on the parameters regime, where a well-localized excitation can be transported
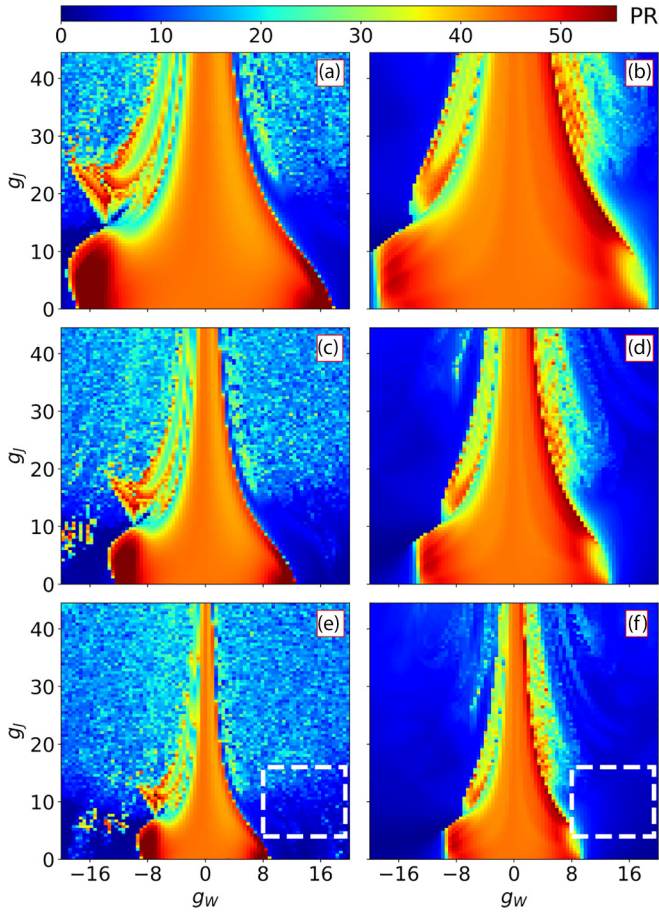
FIG. 4. Color-encoded participation ratio $R_P(t_f)$, Eq. (26), at the final evolution time for a broad range of coupling strengths, $g_J \in [0, 45]$ and $g_W \in [-20, 20]$, in the presence of optical (left column, $\eta = 0$) and acoustic phonons (right column, $\eta = 1$). Each row corresponds to a specific value of the effective mass m_{eff}. Panels (a),(b) correspond to $m_{\text{eff}} = 2$, panels (c),(d) correspond to $m_{\text{eff}} = 1$, and panels (e),(f) correspond to $m_{\text{eff}} = 0.5$. Across all panels, we observe a mixture of extended states (warm colors) and well-localized, non-spreading wave solutions (dark blue colors). Moreover, decreasing effective mass m_{eff} narrows the delocalized phase. Despite some differences, both types of phonons exhibit qualitatively similar behavior, see the discussion in the main text. The remaining parameters used for this analysis are $\omega_{\text{eff}} = 10$, $J_0 = 1$.

over a long distance. Namely, after identifying stable polaron regimes, we proceed to apply a constant force to investigate the propagation of nonspreading solutions.

For this analysis, we fix $F = 0.2$, $m_{\text{eff}} = 0.5$ and select the coupling strengths within the range $g_J \in [4, 16]$ and $g_W \in [8, 20]$. These regions are indicated by a dashed square in the bottom panels of Fig. 4. The results are presented in Fig. 5. The top row of Fig. 5 illustrates the participation ratio, $R_P(t_f)$, for both optical [Fig. 5(a)] and acoustic [Fig. 5(b)] phonons. In both panels, we observe a shift in the boundary between the extended and localized states due to the presence of the applied force. However, the prevalence of dark blue colors, indicating localized regimes, remains evident. The bottom row of Fig. 5 displays $\xi(t_f)$, as given by Eq. (28).
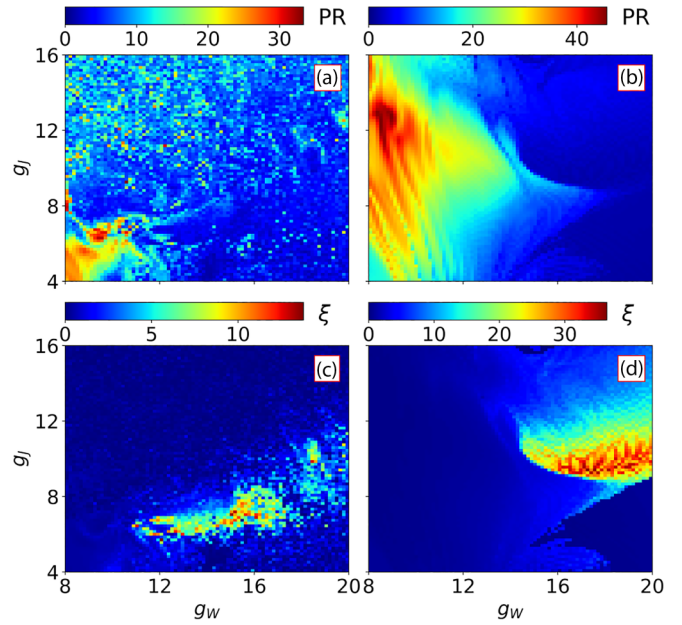

FIG. 5. The influence of a constant force on the propagation of nonspreading solutions. Panels (a),(b) depict the color-encoded participation ratio $R_P(t_f)$ for optical and acoustic phonons, respectively, showing a shift in the boundary between extended and localized states due to the applied force. Panels (c),(d) display color-encoded $\xi(t_f)$, a measure for selecting well-localized solutions propagating in a single direction. Stable transport islands of such solutions are observed, indicated by warm colors. Panel (c) corresponds to optical phonons, while panel (d) corresponds to acoustic phonons. The remaining parameters used for this analysis are $F = 0.2$, $m_{\text{eff}} = 0.5$, $\omega_{\text{eff}} = 10$, $J_0 = 1$. While comparing with Fig. 4 mind a shifted colorscale.

This quantity serves as a measure for selecting well-localized solutions propagating in a single direction. We observe stable transport islands of such solutions, indicated by warm colors. Figure 5(c) corresponds to optical phonons, while Fig. 5(d) corresponds to acoustic phonons.

In Fig. 6, we present an example of transportation of an excitation coupled to phonons under an external force without disorder potential $W = 0$. The left column presents the time evolution of excitation density $|\psi_i|^2$, while the right column presents the evolution of the classical phonon field $|u_i|$. Next, in Fig. 7, we examine the robustness of the nondispersive moving solutions against on-site disorder ϵ_j, as in Eq. (16). The disorder is introduced by assuming ϵ_j to be a pseudorandom variable drawn from a uniform distribution in $[-W/2, W/2]$. Figures 7(a) and 7(b) depict the time propagation of excitations for optical and acoustic phonons, respectively, $W = 0.6$. Figure 7(c) illustrates the center-of-mass position, while Fig. 7(d) presents the participation ratio evaluated at the final evolution time, plotted as functions of the disorder amplitude W. The results are averaged over 200 independent realizations of disorder. Notably, the participation ratio for both acoustic and optical phonons remains relatively constant, providing evidence for the robustness of the polaron self-trapping mechanism, while the center-of-mass positions takes place on a significant distance.
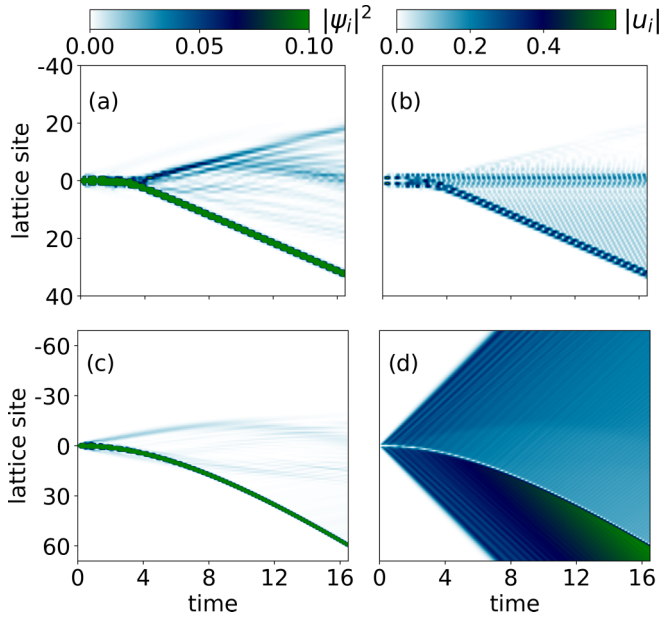
FIG. 6. Transport of an excitation coupled to phonons under an external force $F = 0.2$. Panels (a),(c) present color-encoded time evolution of the excitation density $|\psi_i|^2$, while panels (b),(d) present color-encoded time evolution of the phonon field $|u_i|$. The top row corresponds to optical phonons ($g_W = 16$, $g_J = 7$), while the bottom row corresponds to acoustic phonons ($g_W = 17$, $g_J = 10$).
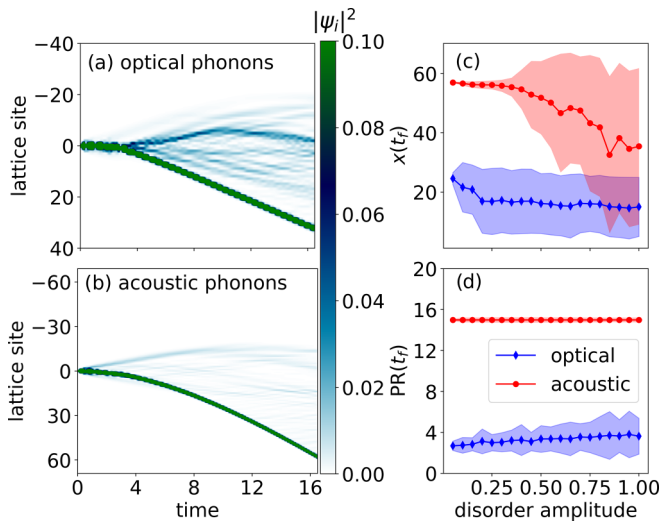

FIG. 7. Robustness of nondispersive moving solutions against on-site disorder, $\epsilon_j \in [-W/2, W/2]$. Panels (a),(b) display color-encoded time evolution of the excitation density $|\psi_i|^2$ for optical ($g_W = 16$, $g_J = 7$) and acoustic ($g_W = 17$, $g_J = 10$) phonons, respectively, disorder strength $W = 0.6$. Panels (c),(d) show the center-of-mass position $x(t_f)$ and the participation ratio $R_P(t_f)$ at the final evolution time t_f, plotted as functions of the disorder amplitude W [top lines (circles) correspond to acoustic phonons, while bottom lines (diamonds) to optical phonons]. Although the center-of-mass positions decreases, a substantial macroscopic transport remains visible. The remaining parameters used for this analysis are $F = 0.2$, $m_{\text{eff}} = 0.5$, $\omega_{\text{eff}} = 10$, $J_0 = 1$.

V. SUMMARY AND CONCLUSION

In summary, we propose a quantum simulator with Rydbeg-dressed atom arrays for SSH-Frölich Hamiltonian allowing studies of polaron formation and dynamics. The interplay between two competing excitation-phonon coupling terms in the model results in a rich dynamical behavior, which we comprehensively analyze. In particular, our findings reveal the presence of asymmetry in Bloch oscillations allowing coherent transport of a well-localized excitation over long distances. Moreover, we compare the behavior of excitations coupled to either acoustic or optical phonons and indicate similar qualitative behavior. Finally, we demonstrate the robustness of phonon-assisted coherent transport to the on-site random potential.

Our analysis is restricted to weak lattice distortions related to a small number of phonons per lattice site, however, the proposed quantum simulator allows the studies of the excitation dynamics in strong distortion limit, as well as studies of a plethora of different scenarios, such as bipolaron and many-polaron dynamics, and investigation of the quantum boomerang effect [81–83] affected by the presence of phonons, both in a single-particle and many-body scenario. We believe that our work opens up additional avenues for research in Rydberg-based quantum simulators.

The data presented in this article are available [84].

[1] L. D. Landau, Electron motion in crystal lattices, Phys. Z. Sowjet. **3**, 664 (1933).

[2] H. Fröhlich, Electrons in lattice fields, Adv. Phys. **3**, 325 (1954).

[3] R. P. Feynman, Slow electrons in a polar crystal, Phys. Rev. **97**, 660 (1955).

[4] R. P. Feynman, R. W. Hellwarth, C. K. Iddings, and P. M. Platzman, Mobility of slow electrons in a polar crystal, Phys. Rev. **127**, 1004 (1962).

[5] T. Holstein, Studies of polaron motion, Ann. Phys. (NY) **8**, 325 (1959).

[6] W. P. Su, J. R. Schrieffer, and A. J. Heeger, Solitons in polyacetylene, Phys. Rev. Lett. **42**, 1698 (1979).

[7] K. A. Chao and Y. Wang, Phonon modes in the Su-Schrieffer-Heeger model for polyacetylene, J. Phys. C **18**, L1127 (1985).

[8] A. J. Heeger, S. Kivelson, J. R. Schrieffer, and W. P. Su, Solitons in conducting polymers, Rev. Mod. Phys. **60**, 781 (1988).

[9] S. Alexandrov and J. T. Devreese, *Advances in Polaron Physics* (Springer, Berlin, 2010).

[10] C. Franchini, M. Reticcioli, M. Setvin, and U. Diebold, Polarons in materials, Nat. Rev. Mater. **6**, 560 (2021).

[11] G. Chuev and V. Lakhno, A polaron model for electron transfer in globular proteins, J. Theor. Biol. **163**, 51 (1993).

[12] D. Čevizović, S. Galović, S. Zeković, and Z. Ivić, Charge transport in the *alpha*-helix proteins, J. Phys.: Conf. Ser. **248**, 012051 (2010).

[13] D. D. Georgiev and J. F. Glazebrook, On the quantum dynamics of Davydov solitons in protein α-helices, Physica A **517**, 257 (2019).

[14] M. Singh, Polaron transport mechanism in DNA, J. Biomater. Sci. Polym. Ed. **15**, 1533 (2004).

[15] L. Vidmar, J. Bonča, M. Mierzejewski, P. Prelovšek, and S. A. Trugman, Nonequilibrium dynamics of the Holstein polaron driven by an external electric field, Phys. Rev. B **83**, 134301 (2011).

[16] R. P. Fornari and A. Troisia, Theory of charge hopping along a disordered polymer chain, Phys. Chem. Chem. Phys. **16**, 9997 (2014).

[17] M. Glück, A. R. Kolovsky, and H. J. Korsch, Wannier–Stark resonances in optical and semiconductor superlattices, Phys. Rep. **366**, 103 (2002).

[18] D. Wiater, T. Sowiński, and J. Zakrzewski, Two bosonic quantum walkers in one-dimensional optical lattices, Phys. Rev. A **96**, 043629 (2017).

[19] M. Magoni, P. P. Mazza, and I. Lesanovsky, Emergent bloch oscillations in a kinetically constrained Rydberg spin lattice, Phys. Rev. Lett. **126**, 103002 (2021).

[20] A. Mezzacapo, J. Casanova, L. Lamata, and E. Solano, Digital quantum simulation of the Holstein model in trapped ions, Phys. Rev. Lett. **109**, 200501 (2012).

[21] V. M. Stojanović, T. Shi, C. Bruder, and J. I. Cirac, Quantum simulation of small-polaron formation with trapped ions, Phys. Rev. Lett. **109**, 250501 (2012).

[22] L. Lamata, A. Mezzacapo, J. Casanova, and E. Solano, Efficient quantum simulation of fermionic and bosonic models in trapped ions, EPJ Quantum Technol. **1**, 9 (2014).

[23] K. Jachymski and A. Negretti, Quantum simulation of extended polaron models using compound atom-ion systems, Phys. Rev. Res. **2**, 033326 (2020).

[24] F. Herrera, M. Litinskaya, and R. V. Krems, Tunable disorder in a crystal of cold polar molecules, Phys. Rev. A **82**, 033428 (2010).

[25] F. Herrera and R. V. Krems, Tunable Holstein model with cold polar molecules, Phys. Rev. A **84**, 051401(R) (2011).

[26] W. Li and I. Lesanovsky, Electronically excited cold ion crystals, Phys. Rev. Lett. **108**, 023003 (2012).

[27] F. Herrera, K. W. Madison, R. V. Krems, and M. Berciu, Investigating polaron transitions with polar molecules, Phys. Rev. Lett. **110**, 223002 (2013).

[28] A. Lampo, S. H. Lim, M. A. Garcia-March, and M. Lewestein, Bose polaron as an instance of quantum Brownian motion, Quantum **1**, 30 (2017).

[29] M. Mehboudi, A. Lampo, C. Charalambous, L. A. Correa, M. A. García-March, and M. Lewenstein, Using polarons for sub-nK quantum nondemolition thermometry in a Bose-Einstein condensate, Phys. Rev. Lett. **122**, 030403 (2019).

[30] F. Scazza, M. Zaccanti, P. Massignan, M. M. Parish, and J. Levinsen, Repulsive Fermi and Bose polarons in quantum gases, Atoms **10**, 55 (2022).

[31] S. Wüster, C. Ates, A. Eisfeld, and J. M. Rost, Excitation transport through Rydberg dressing, New J. Phys. **13**, 073044 (2011).

[32] J. P. Hague and C. MacCormick, Quantum simulation of electron–phonon interactions in strongly deformable materials, New J. Phys. **14**, 033019 (2012).

[33] J. P. Hague, S. Downes, C. MacCormick, and P. E. Kornilovitch, Cold Rydberg atoms for quantum simulation of exotic condensed matter interactions, J. Supercond. Novel Magn. **27**, 937 (2014).

[34] D. Barredo, H. Labuhn, S. Ravets, T. Lahaye, A. Browaeys, and C. S. Adams, Coherent excitation transfer in a spin chain of three Rydberg atoms, Phys. Rev. Lett. **114**, 113002 (2015).

[35] M. Płodzień, T. Sowiński, and S. Kokkelmans, Simulating polaron biophysics with Rydberg atoms, Sci. Rep. **8**, 9247 (2018).

[36] F. Camargo, R. Schmidt, J. D. Whalen, R. Ding, G. Woehl, S. Yoshida, J. Burgdörfer, F. B. Dunning, H. R. Sadeghpour, E. Demler, and T. C. Killian, Creation of Rydberg polarons in a Bose gas, Phys. Rev. Lett. **120**, 083401 (2018).

[37] J. P. Mendonça and K. Jachymski, Quantum simulation of extended electron-phonon-coupling models in a hybrid Rydberg atom setup, Phys. Rev. A **107**, 032808 (2023).

[38] M. Magoni, P. P. Mazza, and I. Lesanovsky, Phonon dressing of a facilitated one-dimensional Rydberg lattice gas, SciPost Phys. Core **5**, 041 (2022).

[39] M. Di Liberto, A. Kruckenhauser, P. Zoller, and M. A. Baranov, Topological phonons in arrays of ultracold dipolar particles, Quantum **6**, 731 (2022).

[40] U. Bhattacharya, T. Grass, A. Bachtold, M. Lewenstein, and F. Pistolesi, Phonon-induced pairing in quantum dot quantum simulator, Nano Lett. **21**, 9661 (2021).

[41] M. Morgado and S. Whitlock, Quantum simulation and computing with Rydberg-interacting qubits, AVS Quantum Science **3**, 023501 (2021).

[42] S. de Léséleuc, V. Lienhard, P. Scholl, D. Barredo, S. Weber, N. Lang, H. P. Büchler, T. Lahaye, and A. Browaeys, Observation of a symmetry-protected topological phase of interacting bosons with Rydberg atoms, Science **365**, 775 (2019).

[43] S. Weber, S. de Léséleuc, V. Lienhard, D. Barredo, T. Lahaye, A. Browaeys, and H. P. Büchler, Topologically protected edge states in small Rydberg systems, Quantum Sci. Technol. **3**, 044001 (2018).

[44] V. Lienhard, S. de Léséleuc, P. Scholl, D. Barredo, T. Lahaye, and A. Browaeys, Experimental realization of a bosonic version of the Su-Schrieffer-heeger (ssh) model with Rydberg atoms, in *Quantum Information and Measurement (QIM) V: Quantum Technologies* (Optica, Washington, DC, 2019), p. F4B.2.

[45] S. E. Anderson, K. C. Younge, and G. Raithel, Trapping Rydberg atoms in an optical lattice, Phys. Rev. Lett. **107**, 263001 (2011).

[46] T. Macrì and T. Pohl, Rydberg dressing of atoms in optical lattices, Phys. Rev. A **89**, 011402(R) (2014).

[47] A. Browaeys and T. Lahaye, Many-body physics with individually controlled Rydberg atoms, Nat. Phys. **16**, 132 (2020).

[48] A. M. Kaufman and K.-K. Ni, Quantum science with optical tweezer arrays of ultracold atoms and molecules, Nat. Phys. **17**, 1324 (2021).

[49] J. T. Wilson, S. Saskin, Y. Meng, S. Ma, R. Dilip, A. P. Burgers, and J. D. Thompson, Trapping alkaline earth Rydberg atoms optical tweezer arrays, Phys. Rev. Lett. **128**, 033201 (2022).

[50] V. Y. F. Leung, D. R. M. Pijn, H. Schlatter, L. Torralbo-Campo, A. L. L. Rooij, G. B. Mulder, J. Naber, M. L. Soudijn, A. Tauschinsky, C. Abarbanel, B. Hadad, E. Golan, R. Folman, and R. J. C. Spreeuw, Magnetic-film atom chip with $10\,\mu m$ period lattices of microtraps for quantum information science with Rydberg atoms, Rev. Sci. Instrum. **85**, 053102 (2014).

[51] K. Henderson, C. Ryu, C. MacCormick, and M. G. Boshier, Experimental demonstration of painting arbitrary and dynamic potentials for Bose–Einstein condensates, New J. Phys. **11**, 043030 (2009).

[52] C. Ates, A. Eisfeld, and J. M. Rost, Motion of Rydberg atoms induced by resonant dipole–dipole interactions, New J. Phys. **10**, 045030 (2008).

[53] J. Honer, H. Weimer, T. Pfau, and H. P. Büchler, Collective many-body interaction in Rydberg dressed atoms, Phys. Rev. Lett. **105**, 160404 (2010).

[54] M. Genkin, S. Wüster, S. Möbius, A. Eisfeld, and J. M. Rost, Dipole–dipole induced global motion of Rydberg-dressed atom clouds, J. Phys. B: At., Mol. Opt. Phys. **47**, 095003 (2014).

[55] J. Zeiher, R. van Bijnen, P. Schauß, S. Hild, J. yoon Choi, T. Pohl, I. Bloch, and C. Gross, Many-body interferometry of a Rydberg-dressed spin lattice, Nat. Phys. **12**, 1095 (2016).

[56] F. Evers and A. D. Mirlin, Anderson transitions, Rev. Mod. Phys. **80**, 1355 (2008).

[57] The next-to-nearest neighbor and higher contributions can be neglected if $\kappa = C_3/(2\hbar\Delta x_0^3)$ is close (but not equal) to 1 due to the divergence of $1/(1 - \bar{U}_{j,j\pm1}^2)$ term, which can be traced to avoided crossings between the perturbed energy eigenvalues [31].

[58] A. S. Davydov, Deformation of molecular crystals at electronic excitation, Phys. Stat. Sol. (B) **36**, 211 (1969).

[59] Y. Zhao, D. W. Brown, and K. Lindenberg, A variational approach to nonlocal exciton–phonon coupling, J. Chem. Phys. **106**, 2728 (1997).

[60] N. Zhou, Z. Huang, J. Zhu, V. Chernyak, and Y. Zhao, Polaron dynamics with a multitude of Davydov D_2 trial states, J. Chem. Phys. **143**, 014113 (2015).

[61] N. Zhou, L. Chen, Z. Huang, K. Sun, Y. Tanimura, and Y. Zhao, Fast, accurate simulation of polaron dynamics and multidimensional spectroscopy by multiple Davydov trial states, J. Phys. Chem. A **120**, 1562 (2016).

[62] Z. Huang, L. Chen, N. Zhou, and Y. Zhao, Transient dynamics of a one-dimensional Holstein polaron under the influence of an external electric field, Ann. Phys. (Leipzig) **529**, 1600367 (2017).

[63] Z. Huang, L. Wang, C. Wu, L. Chen, F. Grossmann, and Y. Zhao, Polaron dynamics with off-diagonal coupling: Beyond the Ehrenfest approximation, Phys. Chem. Chem. Phys. **19**, 1655 (2017).

[64] Y. Zhao, K. Sun, L. Chen, and M. Gelin, The hierarchy of davydov's ansätze and its applications, WIREs Computat. Mol. Sci. **12**, e1589 (2021).

[65] C. Kittel, *Introduction to Solid State Physics*, 8th ed. (Wiley, New York, 2004).

[66] E. H. Lieb and D. W. Robinson, The finite group velocity of quantum spin systems, Commun. Math. Phys. **28**, 251 (1972).

[67] F. Bloch, Über die quantenmechanik der elektronen in kristallgittern, Z. Phys. **52**, 555 (1929).

[68] E. van Nieuwenburg, Y. Baum, and G. Refael, From bloch oscillations to many-body localization in clean interacting systems, Proc. Natl. Acad. Sci. **116**, 9269 (2019).

[69] M. Schulz, C. A. Hooley, R. Moessner, and F. Pollmann, Stark many-body localization, Phys. Rev. Lett. **122**, 040606 (2019).

[70] S. R. Taylor, M. Schulz, F. Pollmann, and R. Moessner, Experimental probes of Stark many-body localization, Phys. Rev. B **102**, 054206 (2020).

[71] Q. Guo, C. Cheng, H. Li, S. Xu, P. Zhang, Z. Wang, C. Song, W. Liu, W. Ren, H. Dong, R. Mondaini, and H. Wang, Stark many-body localization on a superconducting quantum processor, Phys. Rev. Lett. **127**, 240502 (2021).

[72] R. Yao and J. Zakrzewski, Many-body localization of Bosons in an optical lattice: Dynamics in disorder-free potentials, Phys. Rev. B **102**, 104203 (2020).

[73] T. Chanda, R. Yao, and J. Zakrzewski, Coexistence of localized and extended phases: Many-body localization in a harmonic trap, Phys. Rev. Res. **2**, 032039(R) (2020).

[74] R. Yao, T. Chanda, and J. Zakrzewski, Many-body localization in tilted and harmonic potentials, Phys. Rev. B **104**, 014201 (2021).

[75] S. Scherg, T. Kohlert, P. Sala, F. Pollmann, B. H. Madhusudhana, I. Bloch, and M. Aidelsburger, Observing non-ergodicity due to kinetic constraints in tilted Fermi-Hubbard chains, Nat. Commun. **12**, 4490 (2021).

[76] W. Morong, F. Liu, P. Becker, K. S. Collins, L. Feng, A. Kyprianidis, G. Pagano, T. You, A. V. Gorshkov, and C. Monroe, Observation of Stark many-body localization without disorder, Nature (London) **599**, 393 (2021).

[77] T. Kohlert, S. Scherg, P. Sala, F. Pollmann, B. Hebbe Madhusudhana, I. Bloch, and M. Aidelsburger, Exploring the regime of fragmentation in strongly tilted Fermi-Hubbard chains, Phys. Rev. Lett. **130**, 010201 (2023).

[78] H. Nazareno and P. de Brito, Bloch oscillations as generators of polarons in a 1d crystal, Physica B: Condens. Matter **494**, 1 (2016).

[79] Y. Li, X. J. Liu, J. Y. Fu, D. S. Liu, S. J. Xie, and L. M. Mei, Bloch oscillations in a one-dimensional organic lattice, Phys. Rev. B **74**, 184303 (2006).

[80] R. J. Bell and P. Dean, Atomic vibrations in vitreous silica, Discuss. Faraday Soc. **50**, 55 (1970).

[81] T. Prat, D. Delande, and N. Cherroret, Quantum boomeranglike effect of wave packets in random media, Phys. Rev. A **99**, 023629 (2019).

[82] J. Janarek, J. Zakrzewski, and D. Delande, Many-body quantum boomerang effect, Phys. Rev. B **107**, 094204 (2023).

[83] R. Sajjad, J. L. Tanlimco, H. Mas, A. Cao, E. Nolasco-Martinez, E. Q. Simmons, F. L. N. Santos, P. Vignolo, T. Macrì, and D. M. Weld, Observation of the quantum Boomerang effect, Phys. Rev. X **12**, 011035 (2022).

[84] A. Kosior, S. Kokkelmans, M. Lewenstein, J. Zakrzewski, and M. Płodzień, https://doi.org/10.5281/zenodo.10848881.

Correction: The omission of a data availability statement and reference has been fixed.